Research Article Summary

In situ collection of dust grains falling from Saturn's rings into its atmosphere

Hsiang-Wen Hsu, Jürgen Schmidt, Sascha Kempf, Frank Postberg, Georg Moragas-Klostermeyer, Martin Seiß, Holger Hoffmann, Marcia Burton, ShengYi Ye, William S. Kurth, Mihály Horányi, Nozair Khawaja, Frank Spahn, Daniel Schirdewahn, James O'Donoghue, Luke Moore, Jeff Cuzzi, Geraint H. Jones, Ralf Srama*

The list of author affiliations is available in the full article.
**Corresponding author. Email: sean.hsu@ lasp.colorado.edu*

INTRODUCTION: During the Cassini spacecraft's Grand Finale mission in 2017, it performed 22 traversals of the 2000-km-wide region between Saturn and its innermost D ring. During these traversals, the onboard cosmic dust analyzer (CDA) sought to collect material released from the main rings. The science goals were to measure the composition of ring material and determine whether it is falling in- to the planet's atmosphere.

RATIONALE: Clues about the origin of Saturn's massive main rings may lie in their composition. Re- mote observations have shown that they are formed primarily of water ice, with small amounts of other materials such as silicates, complex organics, and nanophase hematite. Fine-grain ejecta generated by hypervelocity collisions of inter- planetary dust particles (IDPs) on the main rings serve as microscopic samples. These grains could be examined in situ by the Cassini spacecraft during its final orbits. Deposition of ring ejecta into Saturn's atmosphere has been suggested as an explanation for the pattern of ionospheric H^+_3 infrared emission, a phenomenon known as ring rain. Dynamical studies have suggested a preferential transport of charged ring particles toward the planet's southern hemisphere because of the northward offset of Saturn's internal magnetic field. However, the deposition flux and its form (ions or charged grains) remained unclear. In situ characterization of the ring ejecta by the Cassini CDA was planned to provide observational constraints on the composition of Saturn's ring system and test the ring rain hypothesis.

RESULTS: The region within Saturn's D ring is populated predominantly by grains tens of nanometers in radius. Larger grains (hundreds of nanometers) dominate the mass density but are narrowly confined within a few hundred kilometers around the ring plane. The measured flux profiles vary with the CDA pointing configurations. The highest dust flux was registered during the ring plane crossings when the CDA was sensitive to the prograde dust populations (Kepler ram pointing) (see the figure). When the CDA was pointed toward the retrograde direction (plasma ram pointing), two additional flux enhancements appeared on both sides of the rings at roughly the same mag- netic latitude. The south dust peak is stronger and wider, indicating the dominance of Saturn's magnet- ic field in the dynamics of charged nanograins. These grains are likely fast ejecta released from the main rings and falling into Saturn, producing the observed ionospheric signature of ring rain.

We estimate that a few tons of nanometer- sized ejecta is produced each second across the main rings. Although this constitutes only a small fraction (<0.1%) of the total ring ejecta production, it is sufficient to supply the observed ring rain effect. Two distinct grain compositional types were identified: water ice and silicate. The silicate-to-ice ratio varies with latitude; the global average ranges from 1:11 to 1:2, higher than that inferred from remote observations of the rings.

CONCLUSION: Our observations illustrate the interactions between Saturn and its main rings through charged, nanometer-sized ejecta particles. The dominance of nanograins between Saturn and its rings is a dynamical selection effect, stemming from the grains' high ejection speeds (hundreds of me- ters per second and higher) and Saturn's offset magnetic field. The presence of the main rings modifies the effects of the IDP infall to Saturn's atmosphere. The rings do this asymmetrically, leading to the distribution of the ring rain phenomenon. Confirmed ring constituents include water ice and silicates, whose ratio is likely shaped by processes associated with ring erosion processes and ring-planet interactions.

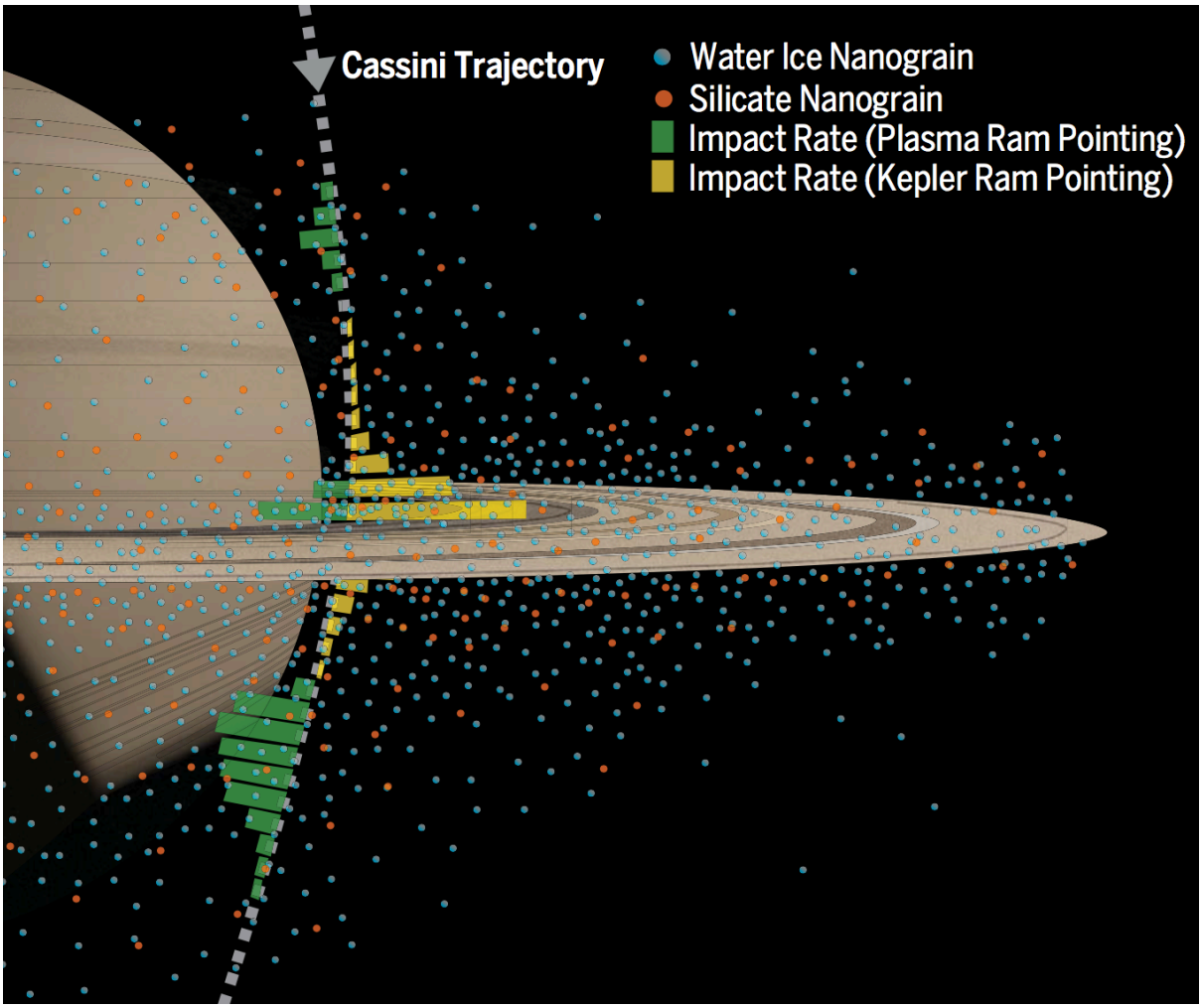

Schematic view of the nanometer-sized ring ejecta environment in the vicinity of Saturn. CDA measurements were taken during Cassini's Grand Finale mission. The measured dust flux profiles, presented by the histograms along the spacecraft trajectory, show different patterns depending on the instrument pointing configuration. The highest dust flux occurred at the ring plane under Kepler ram pointing (yellow). The profiles registered with plasma ram pointing (green) show two additional, mid-latitude peaks at both sides of the rings with substantial north-south asymmetry. This signature in the vertical profiles indicates that the measured nanograins in fact originate from the rings and are whirling into Saturn under the dynamical influence of the planet's offset magnetic field. Blue and orange dots represent the two grain composition types identified in the mass spectra, water ice and silicate, respectively.

Research Article

In situ collection of dust grains falling from Saturn's rings into its atmosphere

Hsiang-Wen Hsu[1], Jürgen Schmidt[2], Sascha Kempf[1], Frank Postberg[3,4], Georg Moragas-Klostermeyer[5], Martin Seiß[6], Holger Hoffmann[6], Marcia Burton[7], ShengYi Ye[8], William S. Kurth[8], Mihály Horányi[1], Nozair Khawaja[3,4], Frank Spahn[6], Daniel Schirdewahn[6], James O'Donoghue[9], Luke Moore[10], Jeff Cuzzi[11], Geraint H. Jones[12,13], Ralf Srama[5,14]*

[1]*Laboratory for Atmospheric and Space Physics, University of Colorado–Boulder, Boulder, CO, USA.*
[2]*Astronomy Research Unit, University of Oulu, Oulu, Finland.*
[3]*Institut für Geowissenschaften, Universität Heidelberg, Heidelberg, Germany.*
[4]*Institut für Geologische Wissenschaften, Freie Universität Berlin, Berlin, Germany.*
[5]*Institut für Raumfahrtsysteme, Universität Stuttgart, Stuttgart, Germany.*
[6]*Institut für Physik und Astronomie, Universität Potsdam, Potsdam, Germany.*
[7]*Jet Propulsion Laboratory, Pasadena, CA, USA.*
[8]*Department of Physics and Astronomy, University of Iowa, Iowa City, IA, USA.*
[9]*NASA Goddard Space Flight Center, Greenbelt, MD, USA.*
[10]*Center for Space Physics, Boston University, Boston, MA, USA.*
[11]*NASA Ames Research Center, Moffett Field, CA, USA.*
[12]*Mullard Space Science Laboratory, University College London, Holmbury St. Mary, Dorking, UK.*
[13]*The Centre for Planetary Sciences at University College London/Birkbeck, London, UK.*
[14]*Center for Astrophysics, Space Physics, and Engineering Research, Baylor University, Waco, TX, USA.*

**Corresponding author. Email: sean.hsu@lasp.colorado.edu*

Saturn's main rings are composed of >95% water ice, and the nature of the remaining few percent has remained unclear. The Cassini spacecraft's traversals between Saturn and its innermost D ring allowed its cosmic dust analyzer (CDA) to collect material released from the main rings and to characterize the ring material infall into Saturn. We report the direct in situ detection of material from Saturn's dense rings by the CDA impact mass spectrometer. Most detected grains are a few tens of nanometers in size and dynamically associated with the previously inferred "ring rain." Silicate and water-ice grains were identified, in proportions that vary with latitude. Silicate grains constitute up to 30% of infalling grains, a higher percentage than the bulk silicate content of the rings.

Infrared and radio observations (1–5) have shown that Saturn's A and B rings are composed mostly (95 to 99%) of water ice, whereas in the less dense C ring and the Cassini Division the non-icy component can be higher, up to 10% in the C ring (5–7). Because of the rings' large surface-to-mass ratio, the evolution of the ring composition is dominated by the infall of material from interplanetary space, which is composed primarily of silicates and carbon-rich organics (8). The radial density profile of the rings is shaped by various dynamical processes, including viscous spreading, resonances with satellites, intrinsic instabilities, and ballistic transport (5, 9–13) of ejecta released by impacts of interplanetary

dust particles on the rings (14). The latter process is primarily responsible for redistributing and mixing the icy and non-icy material across the rings, as well as for the formation of sharp inner A and B ring edges (10, 15). A fraction of the material released by erosion from the rings is expected to fall into Saturn's atmosphere as "ring rain" (16–18). Charged particles from the rings, in the form of ions or nanoparticles, gyrate and bounce along the planet's magnetic field lines and preferentially migrate into Saturn's southern atmosphere (19–25). How- ever, whether the infalling mass flux is sufficient to drive the observed atmospheric processes and whether the infall occurs in the form of ions or dust remain unclear.

We report the in situ detection of nanograins originating from Saturn's main rings by the cosmic dust analyzer (CDA) (26) during Cassini's traversals through the region between the atmosphere and the innermost D ring [1.11 to 1.24 Saturn radii (R_S) = 60,268 km], as shown in Fig. 1. Previously, Cassini instruments observed nanograins that were emerging from the E ring region and evolving into interplanetary space (27–29) and that were directly within the Enceladus ice particle plume (30). From the 22 spacecraft crossings of the inner D ring region during Cassini's Grand Finale mission phase (26 April 2017 to 15 September 2017), eight orbits were useful for CDA measurements because of the optimized instrument pointing (table S1). The spacecraft speed relative to the dust grains was more than 30 km s^{-1} around the closest approach (peri- apsis). The CDA mass analyzer (MA), a linear impact time-of-flight mass spectrometer, pro- vides elemental compositional information for grains with radii in excess of a few nanometers striking the detector (26). The CDA's high rate detector (HRD), a foil detector for characterizing dense dust environments (26), measured the flux of grains in excess of 600 nm in radius during the traversals.

Grain composition

The MA recorded more than 2700 impact mass spectra during the eight inner D ring traversals favorable for CDA measurements. Of these spectra, 78% are very faint and at most show only peaks in the mass spectra associated with the chemical analyzer target (CAT) (made of rhodium) and its known contaminants, Rh^+, C^+, Na^+, and K^+ (31). These spectra do not provide conclusive compositional information about the impacting particle but do provide evidence for the number of impacts by the smallest detectable grains. The remaining 22% of the spectra exhibit peaks associated with particle constituents with sufficient signal-to-noise ratio for a compositional analysis. We identified two distinct compositional types: water ice and silicate (Fig. 2). Ice grains are identified by the presence of at least two of the following water cations: O^+, OH^+, H_2O^+, and H_3O^+. Identification of silicate grains requires a mass peak at 28 u (where u is the atomic mass unit), consistent with Si^+, and at least one additional mass line (Mg^+, Ca^+, or Fe^+) from metallic cations other than Na^+ and K^+. In total, we identified 422 water-ice–type and 214 silicate-type particles, all recorded around the passage of the ring plane within ±50° latitude (see Fig. 1 for the geometry). We did not identify any nanograins composed predominantly of iron, iron oxide, or an organic material. Because of the expected frac- tionation of larger organic molecules at the high impact velocities during these measurements, low- mass organic fragment cations at 12 u (C^+) or 13 u (CH^+) might overlap with the carbon contamination of the CDA impact target (31), curtailing our capability to identify minor organic constituents. The impact charge signals of the water-ice and silicate particles are similar in both amplitude and distribution (see supplementary text). On the basis of the impact charge, which depends linearly on the grain mass for collisions at the same speed (32), the majority of the detected grains are smaller than 50 nm. Taking into ac- count the material-dependent impact charge yield, the CDA target contamination, and simulations of the dynamics of these small grains, we conclude that the ice-to-silicate number ratio of 2:1 translates into a mass ratio of the ice

and silicate grains between 2:1 and 11:1 (see supplementary text). The overall silicate nanograin mass frac- tion as seen by the CDA interior to the D ring ranges from 8 to 30%, which is higher than the concentration of non-ice components in the rings inferred from either optical or microwave measurements (6, 7, 33).

Spatial distribution

The ring plane crossings of the 22 Grand Finale orbits occurred near local noon. The spacecraft always approached the rings from the north and reached periapsis about 10 min after crossing the ring plane at a latitude of 6° south (Fig. 1). The orbits also traversed the magnetic field lines connecting the planet to its main rings when the spacecraft was within ±50° from the ring plane. The high dust impact speed of ~30 km s^{-1} enabled the MA to detect grains as small as tens of nanometers. In contrast, the HRD was sensitive to grains with radii larger than 600 nm. Overall, the CDA was sensitive to dust impacts when the instrument was oriented either toward the Kepler ram direction (i.e., the impact direction of grains moving in circular bound, prograde orbits) or toward the plasma ram direction (i.e., the flow direction of plasma co-rotating with Saturn's magnetic field). In total, the CDA obtained dust density profiles during five orbits with Kepler ram and three orbits with plasma ram pointing (see supplementary text). Because
the CDA was not calibrated for such high impact speeds, the grain size and impact speed cannot be directly derived from the recorded impact charge waveforms (27). We corrected the MA detection rate, which was frequently close to saturation (approximately one impact per second), for instrumental dead-time effects (34).

The MA detections reveal that the 2000-km-wide gap between Saturn's cloud tops and the inner rim of the D ring is populated by grains a few tens of nanometers in radii. The MA impact rate profiles strongly depend on the instrument orientation (Fig. 3, A and B). We observed the impact rate maximum at the time of the ring 0.6 plane crossing during all CDA orbits with Kepler ram instrument orientation. The observed peak rates between 7 and 17 impacts per second correspond to a nanograin number density of 3.5×10^{-2} to 8.5×10^{-2} m^{-3}.

The HRD foil detector was sensitive to larger grains moving in Keplerian orbits and registered 13 particles of >600 nm close to the ring plane, which corresponds to a number density of $(2 \pm 1) \times 10^{-4}$ m^{-3} (Fig. 3C). The Cassini Radio and Plasma Wave Science instrument (RPWS) (35), which was sensitive to plasma signals created by dust impacts onto the spacecraft, had a similar-size-threshold HRD (36). The full widths at half maximum (FWHMs) of the diffuse dust ring interior to the D ring derived from RPWS (37) and HRD data are 300 and 900 km, respectively (Fig. 3C). RPWS provided a more detailed ring structure profile because of its higher temporal resolution, which explains the differences in the derived ring thickness. Given the instrument dead-time effects (34), MA is biased against sampling the larger grains detected by the HRD and RPWS because of their lower number density. We focus on the MA nanograin measurements and their implications below, but the mass density of larger grains is one to two orders of magnitude higher.

For orbits with plasma ram orientation, the MA rate shows two broader peaks in addition to the peak in the ring plane, one on each side of the rings (Fig. 3B). They are centered at roughly the same magnetic latitude north and south, corresponding to L = 1.35 ($L = r/R_S$, which depicts the dipolar magnetic field line piercing the planet's symmetry plane at a radial distance r), which suggests Lorentz force–driven dust dynamics and the main rings as the dust source. We also observed a pronounced north-south asymmetry of the MA count rate, which we attributed to the northward offset of Saturn's magnetic dipole: The south dust peak

is two to three times stronger and much broader than the north peak. Generally, the peak impact rate was an order of magnitude lower than that during Kepler ram orbits.

The fraction of ice nanograins also varies with latitude (Fig. 4A), decreasing from 70 to 90% near the ring plane to ~40% at ~30° latitude, beyond which the small number of detections is insufficient to determine the fraction. In the northern hemisphere, the nanograin density profile is similar to the H^+_3 emission derived from infrared images of Saturn's atmosphere (16–18) (Fig. 4B). The latitudinal H^+_3 emission pattern is indicative of ring material infalling through magnetic connection (ring rain).

Nanograin dynamics

Because the charge-to-mass ratio of the nanograins is high, their dynamics are dominated by the Lorentz force rather than gravity. Thus, a model based on gravitational accelerations alone is not adequate to describe the orbital evolution of such grains. We have developed a numerical model that follows the dynamical evolution of nanograins from their origin on the surface of the main rings, as impact ejecta produced from exogenous hypervelocity collisions, until they are lost to Saturn or the rings or they have moved beyond 2.5 R_S. The model includes relevant forces acting on charged grains: gravity, Lorentz force, and atmospheric drag (38). We employ the axisymmetric Z3 model for describing Saturn's magnetic field (39). The instantaneous grain charge resulting from the interaction with the ambient plasma environment and solar ultraviolet radiation is allowed to vary along the grain orbit. We use a plasma model, which includes Saturn's ionosphere (40) and a simple ring ionosphere (38). By building up a large library of test particle trajectories, our model predicts the nanograin flux and number density near Saturn's main rings (Fig. 1B).

The measured number of ions created by the nanograin impacts on the CDA's rhodium target indicates that the grains have to be smaller than ~50 nm. From comparison to the dust dynamics model, we find that grains with radii of ~15 to 20 nm best reproduce the rate profiles obtained during Kepler ram and plasma ram orbits (Fig. 3) (38). Larger grains are less influenced by the Lorentz force so cannot reach the midlatitudes observed during the plasma ram orbits. Charged grains smaller than 15 nm, on the other hand, are dynamically dominated by the Lorentz force and would populate the entire region, which is not consistent with the observed number density enhancements at the midlatitudes. It is unlikely for the CDA to detect grains smaller than ~5 nm at an impact speed of 30 km s^{-1}. Nanograins with radii of ~20 nm move mostly in the prograde direction and are detected predominantly during Kepler ram orbits. Because of their substantial charge-to-mass ratio, the particles gyrate like an ion along the planetary magnetic field lines. Toward higher latitudes, charged grains are deflected when they reach their magnetic mirror points, where their motion parallel to the field line is reversed. Because the grains' velocity component perpendicular to the magnetic field lines increases toward their mirror points, the nanograin flux arriving from the plasma ram direction is enhanced at the midlatitudes.

The spatial distribution of the nanograins also depends strongly on the grains' initial speed—the speed at which the freshly created nanograin ejecta are jettisoned off the surfaces of the main rings. We find that the ejection speed needs to be larger than a few hundred meters per second to match the rate profiles of the Kepler ram orbits, and it needs to be several thousand meters per second to reproduce the northern peak of the plasma ram orbits. The required high ejection speeds are consistent with data from previous theoretical studies (22) and have been observed in laboratory experiments (impact jetting) (41, 42). The ejection speed is likely to be larger for smaller ejecta (43, 44), implying much higher ejection speeds for nanograins than for micrometer-sized and larger ejecta, which fuel the ballistic transport (10, 15).

Nanograin origin

Our best-fitting simulations of the MA impact rate during Kepler ram orbits indicate that 40% of the detected grains originate from the optical- ly thick B ring, 50% from the C ring, and the rest from the A and D rings, as well as the Cassini Division. The ratio between grains from the B ring and those from the C ring arriving at the Cassini's trajectory is almost constant, implying that the latitudinal variation of the ice fraction (Fig. 4A) is not due to the rings' composition. This conclusion is supported by the much higher ice fraction inferred for the C ring (6) than the two-third fraction that the CDA observed for nanograins. The difference is even larger for the A and B rings. The higher abundance of sili- cate grains seen in the nanograin ejecta population is a consequence of the ejecta production mechanism itself or a shorter lifetime of ice ejecta or a combination of both effects. The pro- cesses responsible for reducing the ice fraction in nanometer-sized ejecta as well as the latitudinal variation remain unclear.

Nature of the ring rain

Our simulations demonstrate that the CDA MA observed charged nanograins on their way from the surfaces of Saturn's main rings into the planet's atmosphere. The match between the MA rates and the H3+ latitudinal emission profile (Fig. 4B) is indicative of the CDA observing a ring rain composed of nanograins.

During their high-speed entry into Saturn's atmosphere, nanograins are expected to ablate and their material to be deposited as neutral atoms or molecules into the atmosphere. These additional neutrals reduce the local electron density, leading to a local accumulation of H^+_3 . Models of the atmospheric capture of 10-nm ice particles predict their mass deposition near an altitude of 2000 km above the level of 1-bar pressure in Saturn's atmosphere (45). The deposited nanograin material would then diffuse down- ward and interact with the ionosphere, prolonging the lifetime of H^+_3 (46, 47).

We estimate from our simulation that the mass production rate for ejecta with sizes in the range of tens of nanometers, $s_{ej;nm}$, is 1,800 to 6,800 kg s^{-1} (38). Eighteen percent of these grains arrive at Saturn as ring rain, of which 30% (100 to 370 kg s^{-1}) are deposited in the mid-latitude region. This estimate is more than an order of magnitude higher than the 3 to 20 kg/s of water required to explain the observed H_3 emission (17). Nevertheless, given the uncertainties in the processes related to the ablation and mass deposition [e.g., (45)], our results agree reasonably well with the ring rain mass infall estimation, implying that the observed nanograin population is the cause of the ring rain effect (19, 21, 22).

The presence of the rings alters how the infall of exogenous material into the saturnian system affects the planet's atmosphere. The deposition of ring material through fast ejecta occurs pre- dominantly at the equator and at southern lat- itudes and may also bear seasonal variations (38). Once deposited in the atmosphere, the nano- grains as well as their ablation products likely serve as the nucleation seeds to form clouds and haze. The asymmetric mass deposition might contribute to the higher optical depth of the cloud or haze in Saturn's southern hemisphere (48–50).

Erosion of the rings

The gross erosion time of the rings (t_g~s_0/s_{ej}), defined as the ratio of the rings' surface mass density(s_0) to the ejecta flux (s_{ej}) (10),can be calculated on the basis of the nanograin mass production rate ($s_{ej;nm}$) derived from CDA measurements: $t_{g,nm}$ ~ 1 × 10^8 to 4 × 10^8

years (assuming a ring mass of 2×10^{19} kg). This is longer than the $t_g = 3 \times 10^5$ years derived from ejecta of all sizes (10), implying a mass fraction of 10^{-4} to 10^{-3} for ejecta in the size range of tens of nanometers.

Probing ring-planet interactions with nanodust

During the Cassini Grand Finale mission, the CDA MA collected material from Saturn's main rings. The gap between Saturn and the inner edge of the D ring is deficient in larger, micrometer- sized grains and populated predominantly by tiny ejecta particles tens of nanometers in radius. The grain dynamics are governed by Saturn's internal magnetic field, leading to a north-south asymmetric ring rain composed of nanograins into the planet's atmosphere. Our model calculations indicate that the nanograins are released predominantly from the B and C rings with speeds of a few hundred meters per second up to several kilometers per second. The observed fast population of tiny ejecta likely represents only a small fraction (<0.1%) of the total impact ejecta produced from the rings, and it is negligible regarding the angular momentum transport. However, the characteristic spatial distribution of the nanometer-sized grains resulting from the electromagnetic dynamics makes them an element in the ring-planet interaction, and they are a probe of the ring composition. The high fraction of silicate nanograins in the CDA data, up to one-third of the identified mass spectra, likely does not provide a direct measure of ring composition but is related to ejecta production and the transport of eroding nanograins.

1. G. P. Kuiper, D. P. Cruikshank, U. Fink, The composition of Saturn's rings. Sky Telescope 39, 14 (1970).

2. C. B. Pilcher, C. R. Chapman, L. A. Lebofsky, H. H. Kieffer, Saturn's rings: Identification of water frost. Science 167, 1372–1373 (1970). doi: 10.1126/science.167.3923.1372; pmid: 17778773

3. J. B. Pollack, A. Summers, B. Baldwin, Estimates of the size of the particles in the rings of saturn and their cosmogonic implications. Icarus 20, 263–278 (1973). doi: 10.1016/ 0019-1035(73)90003-1

4. E. E. Epstein, M. A. Janssen, J. N. Cuzzi, Saturn's rings: 3-mm low-inclination observations and derived properties. Icarus 58, 403–411 (1984). doi: 10.1016/0019-1035(84)90086-1

5. J. N. Cuzzi et al., An evolving view of Saturn's dynamic rings. Science 327, 1470–1475 (2010). doi: 10.1126/science.1179118; pmid: 20299586

6. Z. Zhang et al., Cassini microwave observations provide clues to the origin of Saturn's C ring. Icarus 281, 297–321 (2017). doi: 10.1016/j.icarus.2016.07.020

7. Z. Zhang et al., Exposure age of Saturn's A and B rings, and the Cassini Division as suggested by their non-icy material content. Icarus 294, 14–42 (2017). doi: 10.1016/j.icarus.2017.04.008

8. K. L. Thomas, G. E. Blanford, L. P. Keller, W. Klock, D. S. McKay, Carbon abundance and silicate mineralogy of anhydrous interplanetary dust particles. Geochim. Cosmochim. Acta 57, 1551–1566 (1993). doi: 10.1016/0016-7037(93)90012-L; pmid: 11539451

9. R. H. Durisen, An instability in planetary rings due to ballistic transport. Icarus 115, 66–85 (1995). doi: 10.1006/icar.1995.1079

10. J. N. Cuzzi, P. R. Estrada, Compositional evolution of Saturn's rings due to meteoroid bombardment. Icarus 132, 1–35 (1998). doi: 10.1006/icar.1997.5863

11. S. Charnoz, L. Dones, L. W. Esposito, P. R. Estrada, M. M. Hedman, "Origin and evolution of Saturn's ring system," in Saturn from Cassini-Huygens, M. Dougherty, L. Esposito,
S. Krimigis, Eds. (Springer, 2009), chap. 17, pp. 537–575.

12. J. Schmidt, K. Ohtsuki, N. Rappaport, H. Salo, F. Spahn, "Dynamics of Saturn's dense rings," in Saturn from Cassini-Huygens, M. Dougherty, L. Esposito, S. Krimigis, Eds. (Springer, 2009), chap. 14, pp. 413–458.

13. H. N. Latter, G. I. Ogilvie, M. Chupeau, The ballistic transport instability in Saturn's rings – I. Formalism and linear theory. Mon. Not. R. Astron. Soc. 427, 2336–2348 (2012). doi: 10.1111/ j.1365-2966.2012.22122.x

14. M. S. Tiscareno et al., Observations of ejecta clouds produced by impacts onto Saturn's rings. Science 340, 460–464 (2013). doi: 10.1126/science.1233524; pmid: 23620048

15. P. R. Estrada, R. H. Durisen, J. N. Cuzzi, D. A. Morgan, Combined structural and compositional evolution of planetary rings due to micrometeoroid impacts and ballistic transport. Icarus 252, 415–439 (2015). doi: 10.1016/ j.icarus.2015.02.005

16. J. O'Donoghue et al., The domination of Saturn's low-latitude ionosphere by ring 'rain'. Nature 496, 193–195 (2013). doi: 10.1038/nature12049; pmid: 23579676

17. L. Moore, J. O'Donoghue, I. Müller-Wodarg, M. Galand, M. Mendillo, Saturn ring rain: Model estimates of water influx into Saturn's atmosphere. Icarus 245, 355–366 (2015). doi: 10.1016/j.icarus.2014.08.041

18. J. O'Donoghue et al., Redetection of the ionospheric H_3^+ signature of Saturn's "ring rain". Geophys. Res. Lett. 44, 11,762–11,769 (2017). doi: 10.1002/2017GL075932

19. T. G. Northrop, J. R. Hill, Stability of negatively charged dust grains in Saturn's ring plane. J. Geophys. Res. 87 (A8), 6045 (1982). doi: 10.1029/JA087iA08p06045

20. W.-H. Ip, On plasma transport in the vicinity of the rings of Saturn: A siphon flow mechanism. J. Geophys. Res. 88 (A2), 819 (1983). doi: 10.1029/JA088iA02p00819

21. J. E. P. Connerney, Magnetic connection for Saturn's rings and atmosphere. Geophys. Res. Lett. 13, 773–776 (1986).
doi: 10.1029/GL013i008p00773

22. T. G. Northrop, J. E. P. Connerney, A micrometeorite erosion model and the age of Saturn's rings. Icarus 70, 124–137 (1987). doi: 10.1016/0019-1035(87)90079-0

23. W. Tseng, W. Ip, R. E. Johnson, T. A. Cassidy, M. K. Elrod, The structure and time variability of the ring atmosphere and ionosphere. Icarus 206, 382–389 (2010). doi: 10.1016/ j.icarus.2009.05.019

24. C.-M. Liu, W.-H. Ip, A new pathway of Saturnian ring- ionosphere coupling via charged nanograins. Astrophys. J. 786, 34 (2014). doi: 10.1088/0004-637X/786/1/34

25. W.-H. Ip, C.-M. Liu, K.-C. Pan, Transport and electrodynamical coupling of nano-grains ejected from the Saturnian rings and their possible ionospheric signatures. Icarus 276, 163–169 (2016). doi: 10.1016/j.icarus.2016.04.004

26. R. Srama et al., The Cassini Cosmic Dust Analyzer. Space Sci. Rev. 114, 465–518 (2004). doi: 10.1007/s11214-004-1435-z

27. S. Kempf et al., High-velocity streams of dust originating from Saturn. Nature 433, 289–291 (2005). doi: 10.1038/nature03218; pmid: 15662418

28. S. Kempf et al., Composition of saturnian stream particles. Science 307, 1274–1276 (2005). doi: 10.1126/science.1106218; pmid: 15731446

29. H.-W. Hsu et al., Ongoing hydrothermal activities within Enceladus. Nature 519, 207–210 (2015). doi: 10.1038/ nature14262; pmid: 25762281

30. G. H. Jones et al., Fine jet structure of electrically charged grains in Enceladus' plume. Geophys. Res. Lett. 36, L16204 (2009). doi: 10.1029/2009GL038284

31. F. Postberg et al., Discriminating contamination from particle components in spectra of Cassini's dust detector CDA. Planet. Space Sci. 57, 1359–1374 (2009). doi: 10.1016/ j.pss.2009.06.027

32. J. R. Göller, E. Grün, Calibration of the Galileo/Ulysses dust detectors with different projectile materials and at varying impact angles. Planet. Space Sci. 37, 1197–1206 (1989). doi: 10.1016/0032-0633(89)90014-7

33. J. N. Cuzzi et al., HST-STIS spectra and the redness of Saturn's rings. Icarus 309, 363–388 (2018). doi: 10.1016/j.icarus.2018.02.025

34. S. Kempf, Interpretation of high rate dust measurements with the Cassini dust detector CDA. Planet. Space Sci. 56, 378–385 (2008). doi: 10.1016/j.pss.2007.11.022

35. D. A. Gurnett et al., The Cassini radio and plasma wave investigation. Space Sci. Rev. 114, 395–463 (2004). doi: 10.1007/s11214-004-1434-0

36. S.-Y. Ye et al., Properties of dust particles near Saturn inferred from voltage pulses induced by dust impacts on Cassini spacecraft. J. Geophys. Res. Space Phys. 119, 6294–6312 (2014). doi: 10.1002/2014JA020024

37. S.-Y. Ye et al., Dust observations by the Radio and Plasma Wave Science instrument during Cassini's Grand Finale. Geophys.
Res. Lett. 10.1029/2018GL078059 (2018).

38. Materials and methods are available as supplementary materials.

39. M. E. Burton, M. K. Dougherty, C. T. Russell, Saturn's internal planetary magnetic field. Geophys. Res. Lett. 37, L24105 (2010). doi: 10.1029/2010GL045148

40. J. E. Wahlund et al., In situ measurements of Saturn's ionosphere show that it is dynamic and interacts with the rings. Science 359, 66–68 (2018). doi: 10.1126/science.aao4134; pmid: 29229651

41. M. Arakawa, M. Higa, Measurements of ejection velocities in collisional disruption of ice spheres. Planet. Space Sci. 44, 901–908 (1996). doi: 10.1016/0032-0633(95)00119-0

42. Y. Shimaki, M. Arakawa, Experimental study on collisional disruption of highly porous icy bodies. Icarus 218, 737–750 (2012). doi: 10.1016/j.icarus.2012.01.021

43. H. J. Melosh, Impact ejection, spallation, and the origin of meteorites. Icarus 59, 234–260 (1984). doi: 10.1016/0019- 1035(84)90026-5

44. M. Sachse, J. Schmidt, S. Kempf, F. Spahn, Correlation between speed and size for ejecta from hypervelocity impacts. J. Geophys. Res. 120, 1847–1858 (2015). doi: 10.1002/2015JE004844

45. O. Hamil, T. E. Cravens, N. L. Reedy, S. Sakai, Fate of ice grains in Saturn's ionosphere. J. Geophys. Res. 123, 1429–1440 (2018). doi: 10.1002/2017JA024616

46. T. S. Stallard et al., Peak emission altitude of Saturn's H_3^+ aurora. Geophys. Res. Lett. 39, L15103 (2012). doi: 10.1029/ 2012GL052806

47. Y. H. Kim, J. L. Fox, J. H. Black, J. I. Moses, Hydrocarbon ions in the lower ionosphere of Saturn. J. Geophys. Res. 119, 384–395 (2014). doi: 10.1002/2013JA019022

48. L. N. Fletcher et al., Saturn's tropospheric composition and clouds from Cassini/VIMS 4.6–5.1mm nightside spectroscopy. Icarus 214, 510–533 (2011). doi: 10.1016/j.icarus.2011.06.006

49. M. T. Roman, D. Banfield, P. J. Gierasch, Saturn's cloud structure inferred from Cassini ISS. Icarus 225, 93–110 (2013). doi: 10.1016/j.icarus.2013.03.015

50. J. K. Barstow, P. G. J. Irwin, L. N. Fletcher, R. S. Giles, C. Merlet, Probing Saturn's tropospheric cloud with Cassini/VIMS. Icarus 271, 400–417 (2016). doi: 10.1016/j.icarus.2016.01.013

51. D. T. Young et al., Cassini plasma spectrometer investigation. Space Sci. Rev. 114, 1–112 (2004). doi: 10.1007/s11214-004-1406-4

ACKNOWLEDGMENTS

We thank T. Munsat for advice on writing this report. H.-W.H. thanks W.-H. Ip, J.-E. Wahlund, P. Kollmann, J. E. P. Connerney, and W.-L. Tseng for the fruitful discussions. H.-W.H. thanks C.-Y. Wang, Li. Hsu, and Lu. Hsu for their support. Funding: We acknowledge the support from NASA, ESA, and the Cassini project. This work is partially supported by the NASA/ROSES-2015 NNX16AI35G Cassini Data Analysis and Participating Scientist program, the Deutsches Zentrum für Luft- und Raumfahrt (OH 1401), and the Deutsche Forschungsgemeinschaft (Sp384/33-1, Ho5720/1-1). J.S. acknowledges support by the Academy of Finland. F.P. was supported by German Research Foundation (DFG) projects

PO 1015/2-1 and -/3-1. F.P. and N.K. were supported by DFG project PO 1015/4-1 and ERC consolidator grant 724908–Habitat-OASIS. G.H.J. is grateful to the UK Science and Technology Facilities Council for partial support. Author contributions: J.S., S.K., R.S., F.P., M.H., F.S., J.C., M.B., and H.-W.H. outlined the study concept; H.-W.H., G. M.-K., R.S., S.K., M.B., and F.P. designed the CDA observation; S.K., G.M.-K., and R.S. performed the initial data processing; M.S., H.H., and F.S. performed the HRD data analysis; S.Y. and W.S.K. provided the RPWS results; F.P., N.K., and S.K. performed the CDA mass spectra data analyses; H.-W.H., S.K., G.M.-K., R.S., F.S., and D.S. performed the dynamical analyses; H.-W.H., M.H., and S.K. performed the numerical modeling; J.O., L.M., and H.-W.H. contributed to the study of ring-planet interaction; H.-W.H., S.K., J.C., J.S., F.S., and D.S. contributed to the study of the ring ejecta dynamics; G.H.J. provided information about the Cassini plasma spectrometer (CAPS) nanograin detection during the Saturn orbit insertion; all authors discussed the results and commented on the manuscript. Competing interests: None declared. Data and materials availability: The CDA and HRD data are available in the Planetary Data System at https://sbnarchive.psi.edu/pds3/cassini/cda/COCDA_0100/ and https://sbnarchive.psi.edu/pds3/cassini/hrd/cohrd18/, respectively. We analyzed the data from the orbits listed in table S1. The numerical simulation code (in IDL) for modeling the grain dynamics is available at https://github.com/seanhwhsu/PXMD.

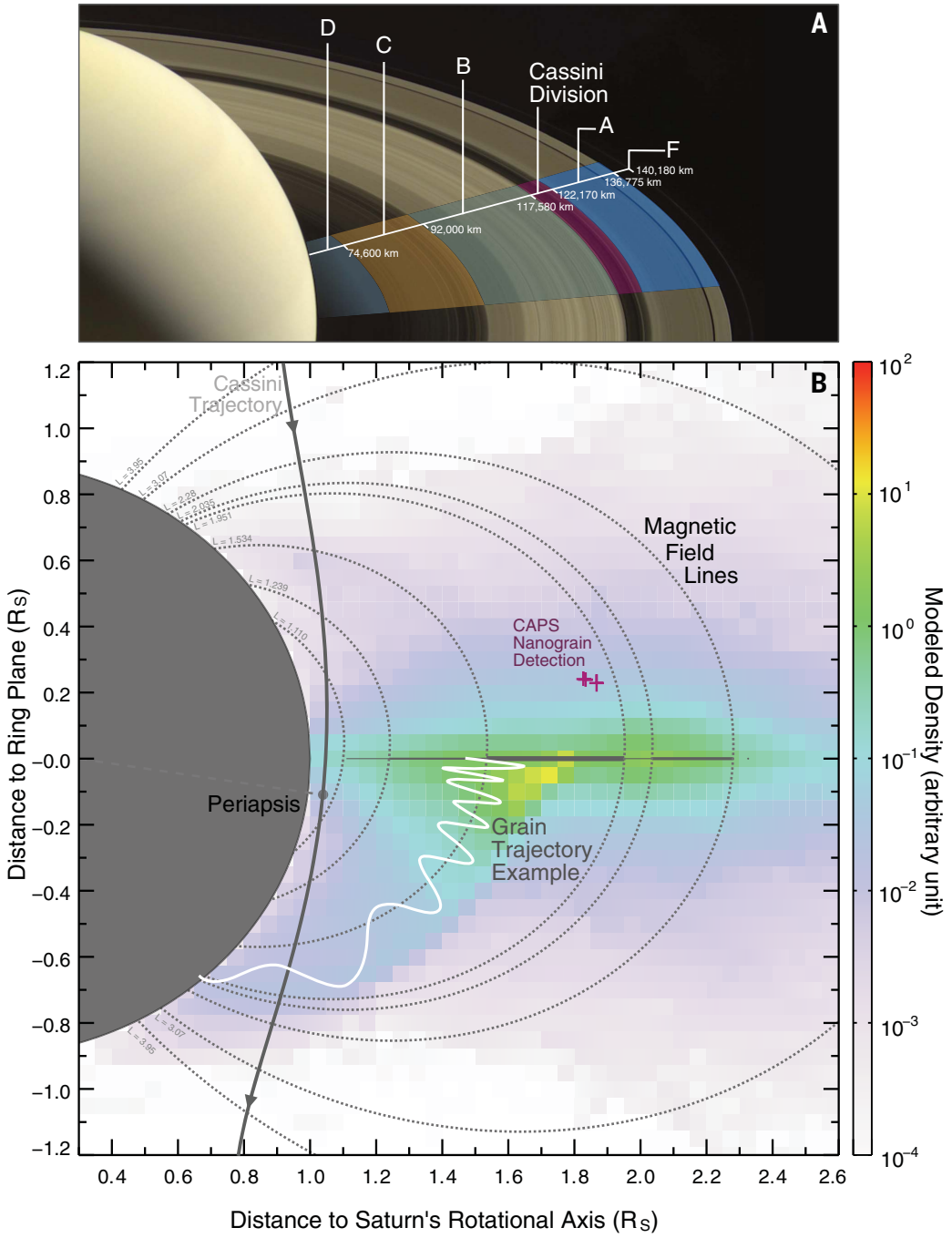

Fig. 1. Edge-on view of a typical Cassini Grand Finale orbit. (A) A mosaic image of Saturn's rings taken by Cassini. (B) The gray curve is the Cassini trajectory around its periapsis, with our model grain density profile in the background. The grid size is 0.05 RS, corresponding to about 300 s of CDA measurements along the trajectory. Dotted curves mark planetary magnetic field lines connecting the edges of the main ring segments D, C, B, and A, as well as the orbits of icy moons Mimas (L = 3.07) and Enceladus (L = 3.95), with Saturn's atmosphere (39). Purple crosses indicate the locations of negatively charged nanograin detections by the Cassini plasma spectrometer (CAPS) (51) during Cassini's Saturn orbit insertion in 2004 near an L shell of 1.9. An example trajectory of a charged nanograin launched from the main rings (white line) demonstrates the strong influence of the Lorentz forces on the grain dynamics, which leads to the grain's deposition in Saturn's southern hemisphere.

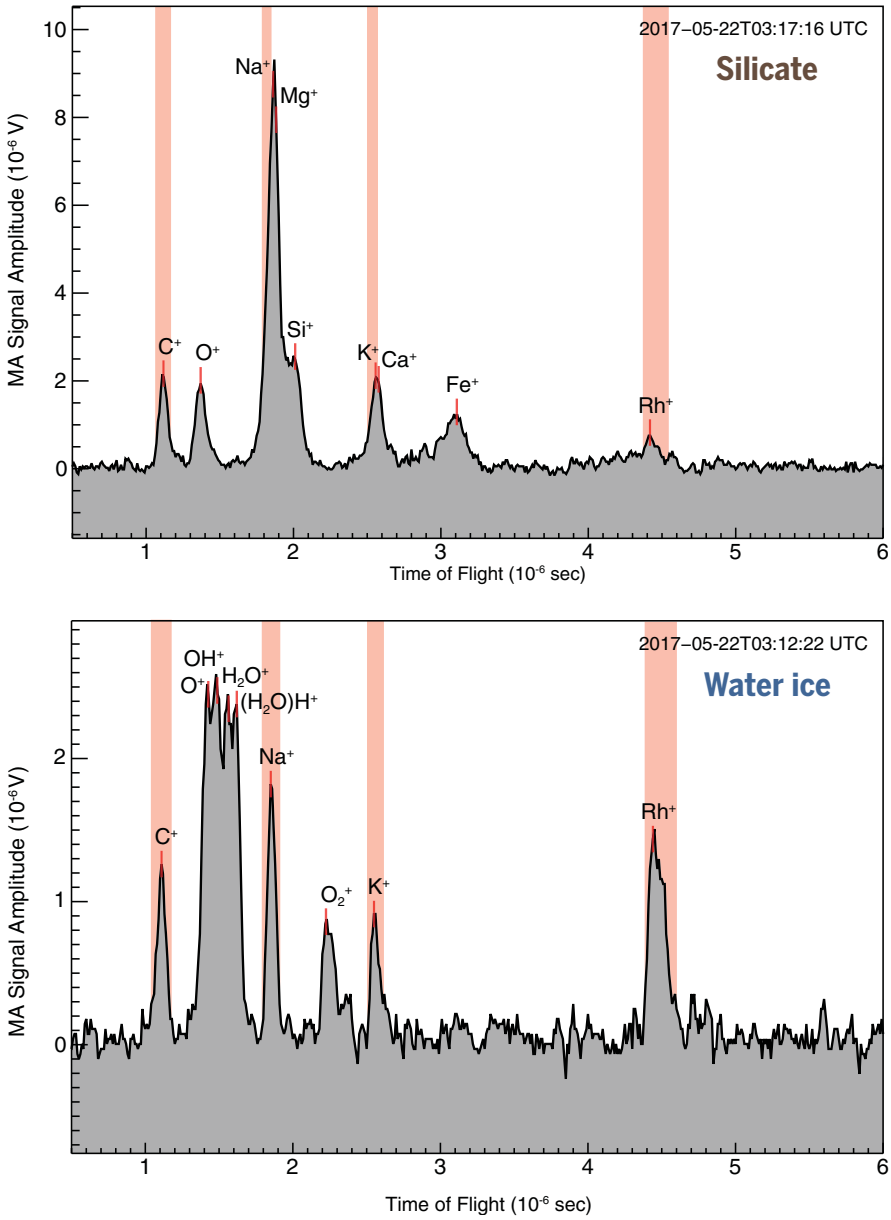

Fig. 2. Example mass spectra for the two nanograin populations detected interior to the D ring. Both mass spectra were recorded over a few minutes around the ring plane crossing of orbit 275 on 22 May 2017 (day 142). Vertical shaded regions indicate mass lines stemming from the CAT (Rh^+) and target contaminants (C^+, Na^+, and K^+). Na^+ and K^+ contamination probably arises from the remains of salt-rich grains that impacted the instrument during prior Enceladus plume traversals (31). However, Na^+ and K^+ cannot be completely ruled out as grain constituents. (Top) Mass spectrum of a silicate nanograin characterized by its Mg^+, Si^+, and Fe^+ mass lines. (Bottom) Mass spectrum of a water-ice nanograin characterized by its O^+, OH^+, H_2O^+, and H_3O^+ mass lines.

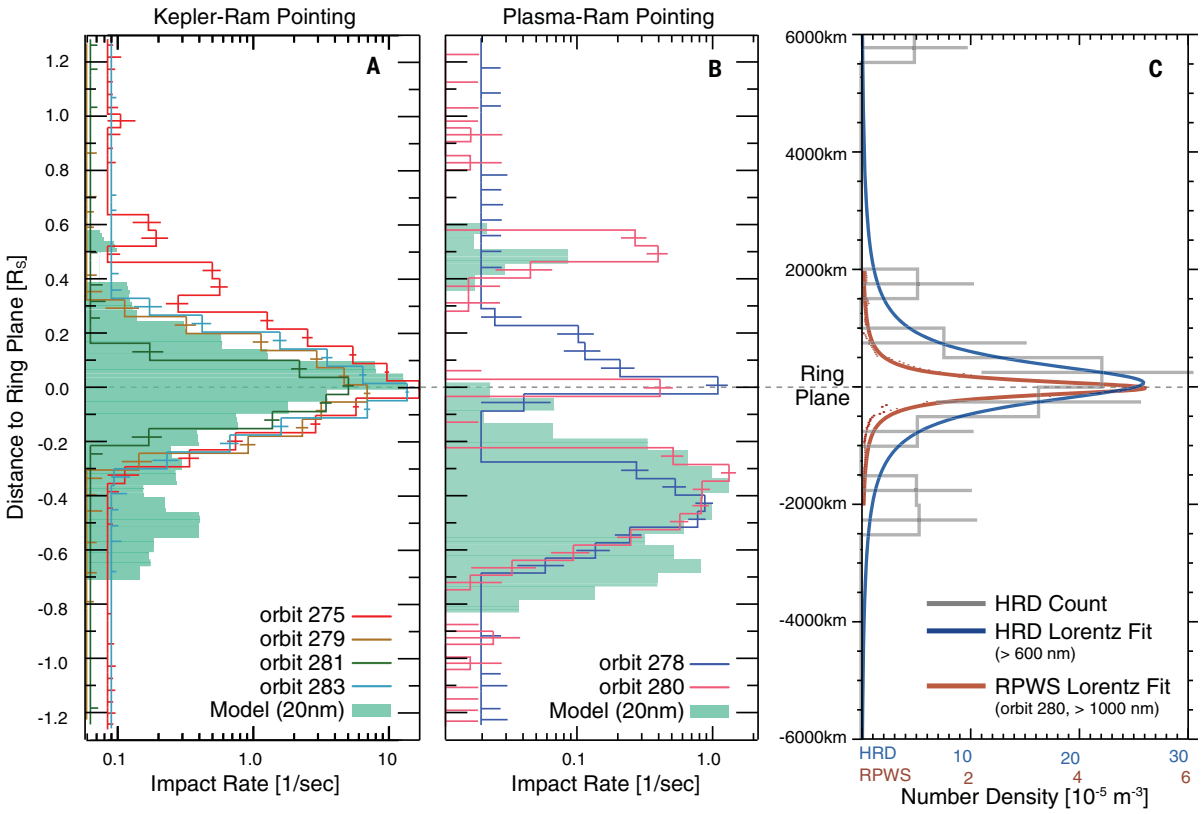

Fig. 3. Vertical density profiles measured by the CDA (MA and HRD) and RPWS. The MA impact rate is plotted as a function of the ring plane distance during (A) Kepler ram and (B) plasma ram orbits. The green histograms are the results of our model calculations for 20-nm grains. The impact rate was generally about 10 times higher during Kepler ram orbits than plasma ram orbits. (C) The profile of ring particles interior to the D ring, measured by the HRD and RPWS (37). The instruments had similar size detection thresholds (600 nm and 1000 nm), but RPWS had a much larger sensitive area and thus a much higher temporal resolution. Overlain are fitted Lorentz density profiles, with vertical FWHMs of 900 km (HRD) and 300 km (RPWS). The RPWS peak density is offset by 4 km below the ring plane. The vertical range occupied by larger ring particles (larger than 600 nm) is about 10 times smaller than that for the nanograins.

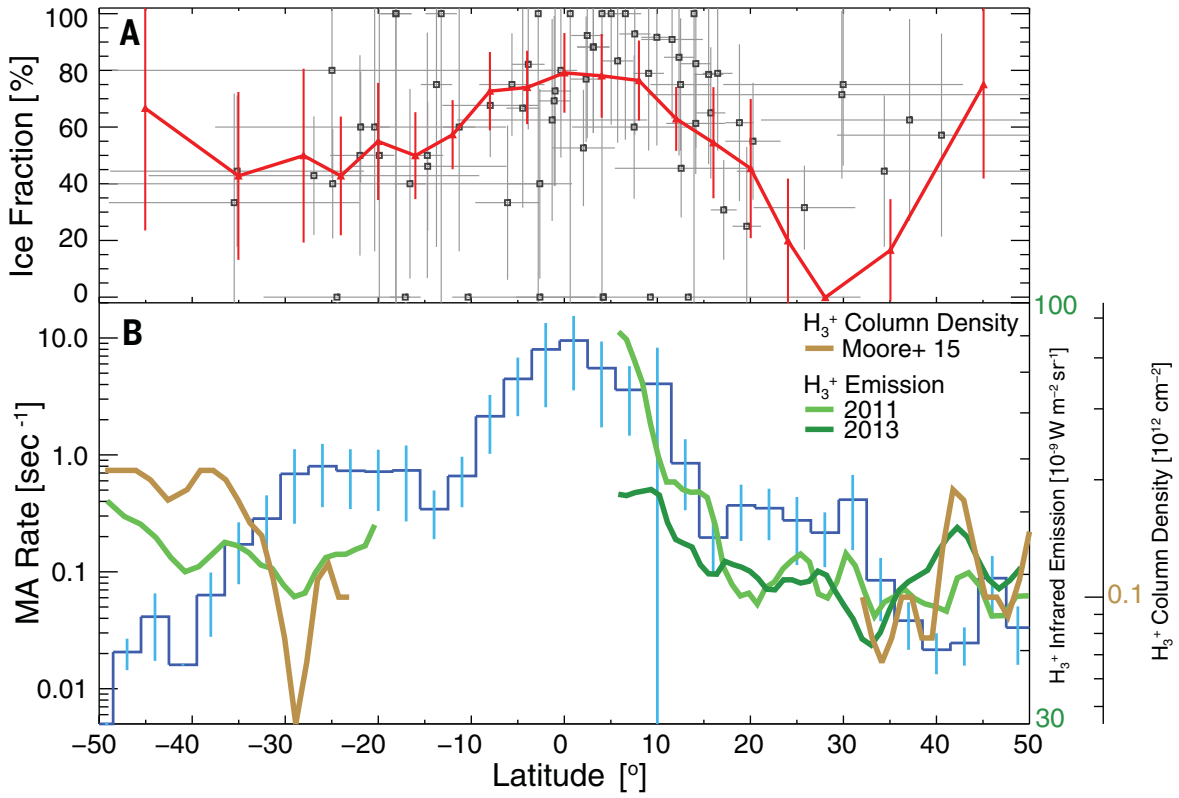

Fig. 4. Ice fraction and impact rate as a function of latitude. (A) The fraction of ice spectra exhibits a dependence on the latitude, with a maximum of 70 to 90% around the ring plane. Squares are dead-time–corrected ice fractions for 50 consecutive spectra; horizontal bars indicate the latitude range of the contributing spectra. The red line is derived directly from the spectrum number fraction without the dead-time correction. Error bars show the uncertainty associated with the counting statistics. (B) Comparison of the latitudinal profiles of the nanograin impact rate (blue histogram) and the H^+_3 infrared emission from Saturn's atmosphere observed between 2011 and 2013 (18) and the corresponding column density (17) (green and gold curves). The MA impact rate is a boxcar average weighted by the number of counts in each bin. The CDA measurements (ice fraction and impact rate) are shown as a function of the latitude of the spacecraft along its trajectory, whereas the H^b_3 profiles are shown as a function of planetocentric latitude on the planet. Away from the ring plane, the latitude
at which nanograins enter the atmosphere is not the same as the latitude of the MA detection along the trajectory. This may explain the shift of pattern in comparing the MA rate and H^+_3 profiles.